Capacitively Sensed Micromachined Hydrophone with Viscous Fluid-Structure Coupling

Robert D. White, Lei Cheng, and Karl Grosh

University of Michigan, Ann Arbor, MI 48109

ABSTRACT

This work presents a novel design for a micromachined, capacitively sensed hydrophone. The design consists of a fluid-filled chamber constrained by two sets of membranes. The "input" membranes are arrayed around the outside of the circular chamber. Incoming sound generates a trapped cylindrical wave, creating mechanically amplified motion of the 1 mm diameter central "sensing" membrane. The membrane material is a LPCVD nitride/oxide/nitride triple-stack with respective film thickness 0.1/0.65/0.1 μm. The chamber is filled with 200 cSt viscosity silicone oil. Fluid-filling eases design constraints associated with submerging the sensor, especially with respect to exterior mass loading. Both silicon-glass anodic bonding and tin-gold solder bonding are used to form the structure, including the 5 μm sensing gap.

The fluid-structure system is computationally modeled using both approximate analytic and numerical techniques. Model results indicate a 28 dB displacement gain between the motion of the "input" membranes and the "sensing" membranes. An off-chip charge amplifier, with a 10 pF integrating capacitor, is used to convert membrane motion into an electrical signal. Mean measured system sensitivity is 0.8 mV/Pa (-180 dB re 1 V/μPa) from 300 Hz-15 kHz with a 1.5 volt applied bias and a 26 dB preamplifier gain. The predicted low frequency sensitivity is 0.3 mV/Pa. The measured sensitivity exhibits considerable scatter below 7 kHz, with a standard deviation of 80%. Laser vibrometry measurements indicate that this scatter may be caused by compliance of the chip mounting scheme. Above 10 kHz, the quiescent noise is -100 dB re 1 $V/\sqrt{Hz}$. Noise characteristics exhibit a 1/f character below 10 kHz, rising to a maximum of -50 dB re 1 $V/\sqrt{Hz}$ at 100 Hz.

Keywords: MEMS, hydrophone, capacitive, condenser, microfabrication, bonding, fluid-structure interaction, viscosity

1. INTRODUCTION

Micromachined capacitively sensed microphones, also called condenser microphones, have been designed and constructed by a number of researchers.[1–4] These microphones operate by sensing fluctuations in the separation between a fixed electrode and a flexible electrode induced by insonification of the flexible membrane. A bias is applied across the gap converting deflections of the sensing membrane to charge which is integrated by a preamplifier to give a voltage output. Sensitivities are generally on the order of 1-20 mV/Pa, depending on the applied bias, size and tension of the membrane, and the details of the preamplifier design. Bandwidths are on the order of 10-20 kHz. If these in-air designs were used as hydrophones, the mass loading introduced by the heavy fluid environment would reduce the bandwidth by approximately a decade (based on the fluid mass loading of a piston and typical mass of the MEMS membranes). To compensate, the tension in the membrane would need to be increased by two orders of magnitude to maintain the same bandwidth, reducing the low frequency sensitivity by two orders of magnitude. Hence, an alternative design was sought.

The design presented in this paper demonstrates a novel approach to dealing with this problem. A fluid chamber is included as part of the MEMS structure. The interaction of this fluid with the membranes increases the dynamic mass of the system, so that additional mass loading from a heavy fluid environment will not influence the sensor bandwidth. The effective system stiffness is increased, by increasing membrane tension and adding the stiffness of the fluid cavity, to maintain a 10 kHz bandwidth. This results in the expected reduction of sensitivity of 2 orders of magnitude. We show that an order of magnitude of sensitivity can be recovered by

Send correspondence to K. Grosh. E-mail: grosh@umich.edu Tel: (734)764-9414

Microfluidics, BioMEMS, and Medical Microsystems III, edited by Ian Papautsky, Isabelle Chartier, Proceedings of SPIE Vol. 5718 (SPIE, Bellingham, WA, 2005)
0277-786X/05/$15 · doi: 10.1117/12.591376

using a unique structure; a ring of "input" membranes with a large area collects sound around the outside of the structure, transmitting a cylindrical pressure wave through the trapped fluid in the chamber, and generating amplified motion of the central sensing membrane (See Figure 1). The achieved sensitivity is 20 dB higher than that achieved by a capacitively sensed hydrophone with a similar preamplifier,[5] and is similar to that achieved by micromachined piezoelectric hydrophones.[6,7] Due to unresolved packaging challenges, the system has yet to be tested in submerged operation, so all experimental results are presented for the system operating in air. However, model results indicate that the sensor will have the same sensitivity and bandwidth for submerged operation as for in–air. In this paper, design, fabrication, modeling, and measurement techniques are discussed along with trade-offs of the current design and potential improvements.

2. DESIGN

The mechanical portion of the micromachined hydrophone, diagrammed in Figure 1, is a square silicon die 1.25 cm on a side. It consists of a 0.5 mm deep, 10 mm diameter fluid chamber, filled with 200 cSt silicone oil. This chamber is constrained on one side by a series of flexible membranes. The center membrane is circular with a 1 mm diameter. Arrayed around the outer portions of the chamber are two rings of 8 arc segments, each subtending 30 degrees, with inner and outer diameters as shown in the figure. The bottom side of the chamber is sealed by bonding on a square Pyrex die 1.25 cm on a side. On the top side, a smaller square Pyrex glass die, 5 mm on a side and 0.5 mm thick, is bonded over the center of the silicon chip. Thin film metal electrodes are fabricated on both the silicon and Pyrex to form a parallel plate capacitor, one side of which is the flexible center membrane.

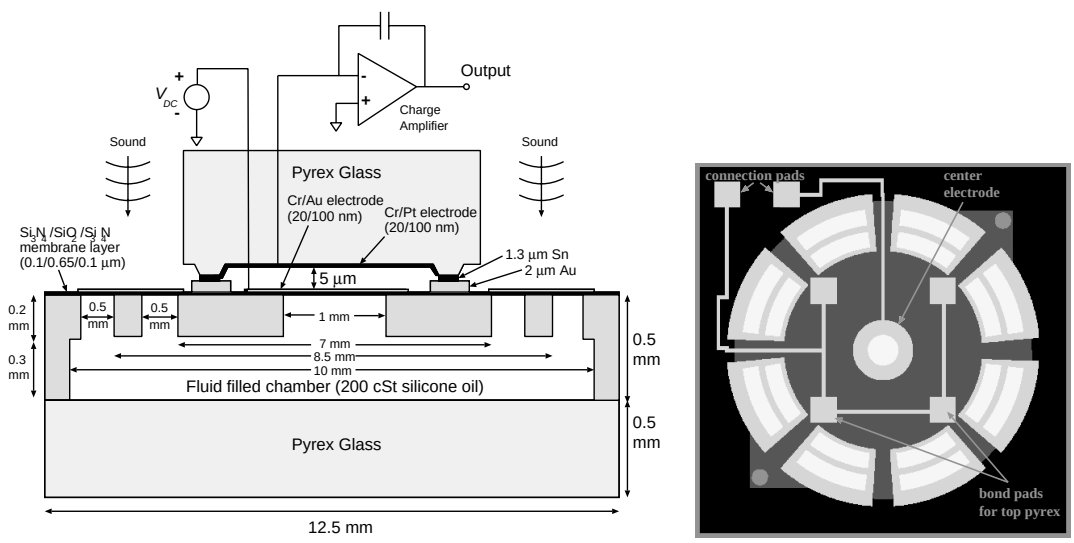

Figure 1. Conceptual diagram of the sensor system showing important geometry. (a) Cross-section showing multi-height fluid chamber and the bonded Pyrex pieces. (b) Top view shows the layout of the metalization, the location of the flexible membranes, and the location of the bonding pads.

Incoming sound excites motion of the outer "input" membranes, generating an acoustic pressure in the fluid chamber. This causes deflection of the center membrane. With a DC bias applied across the two electrodes of the sensing capacitor, deflections result in charge generation. The charge is integrated by a charge amplifier to produce a voltage output.

3. MICROFABRICATION

The fabrication process is diagrammed in Figure 2. The starting substrates are a double-side polished 100 mm diameter, 500 μm thick, <100> oriented, p-type (1-10 Ohm·cm) silicon wafer and a 100 mm diameter, 500 μm

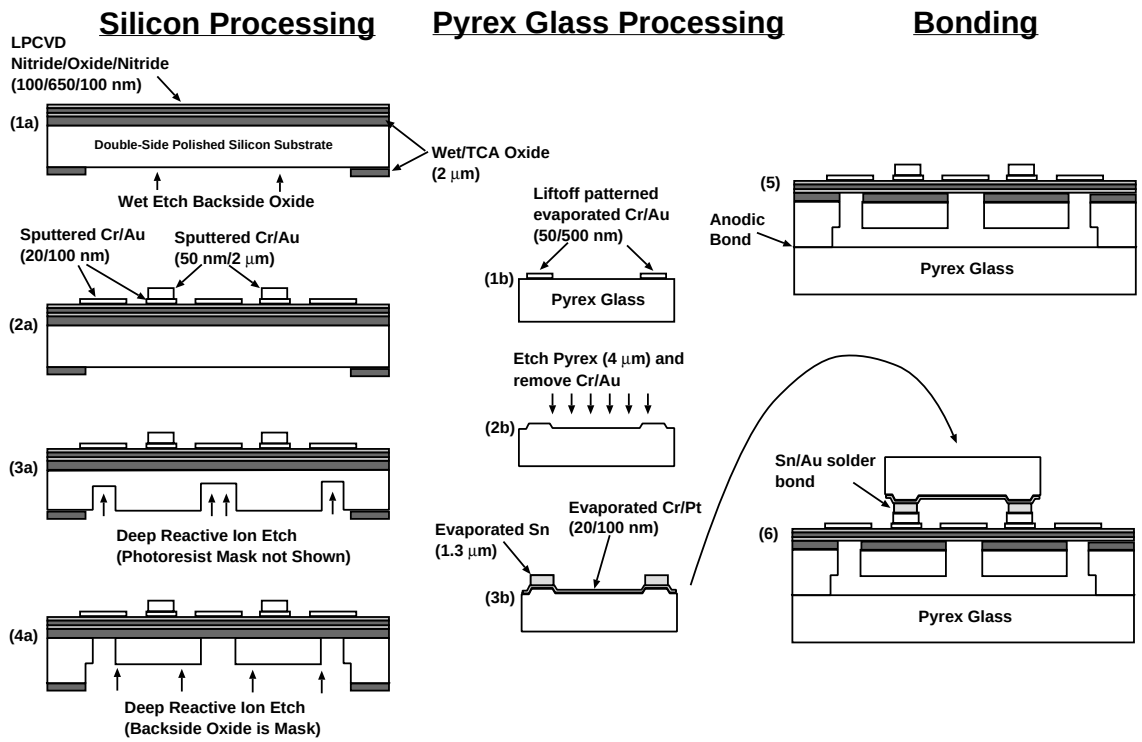

Figure 2. Diagram of the microfabrication process.

thick Pyrex glass wafer. The wafers are first cleaned using an RCA clean for the silicon wafers and a Piranha (1:1 H_2SO_4:H_2O_2) clean for the Pyrex substrates. A 2 μm thick SiO_2 layer is grown on the silicon by thermal oxidation, followed by an LPCVD deposition of the stoichiometric $Si_3N_4/SiO_2/Si_3N_4$ (100/650/100 nm thick) triple-stack membrane layer. The LPCVD films are stripped off the backside using reactive ion etching (RIE). The backside oxide is patterned (wet etch with buffered HF) as a hard mask for a later DRIE step. This step determines the shape of the fluid chamber, as shown in Figure 2. The nitride/oxide/nitride (100/650/100 nm) triple-stack used for the membranes results in a lower net tension than would be present in a purely stoichiometric nitride membrane. Wafer curvature measurements of LPCVD nitride and oxide deposited with the same process indicate residual stresses of 1 GPa (tensile) and 200 MPa (compressive) respectively. Hence, based on the film thicknesses, we expect a membrane tension of approximately 70 N/m (tensile).

Next, vias are etched through all 4 topside insulating films using RIE. These features are not shown in Figure 2. The vias will be used to make contact to the silicon during the anodic bonding step. The metal electrode layer, 20 nm Cr/100 nm Au, is then sputtered onto the silicon frontside and patterned using a liftoff process. A second metal layer, 50 nm Cr/2 μm Au, is sputtered onto the silicon frontside both to make contact through the vias to the bulk silicon, and to provide thick Au on the bond pads for the Sn-Au bonding step. This is also patterned using liftoff resulting in the structure shown in Figure 2 step 2a.

Deep reactive ion etching (DRIE) is used to etch the silicon wafer from the backside using a thick photoresist mask (10 μm AZ9260). This step determines the location of the thin membranes, and is also used to produce deep cleaving lines for separating the wafer into dies. The etch is timed to create approximately 300 μm deep channels, as shown in see Figure 2 step 3a. The silicon wafer is cleaved into individual dies along the DRIE etched cleaving lines, and the photoresist mask is removed. The individual dies are then mounted to a handle wafer using thick photoresist, and etched through using DRIE, stopping on the 2 μm thermal oxide. The 2 μm thermal oxide on the backside serves as an etch mask during this step as shown in Figure 2 step 4a. The two-stage DRIE etch creates both the thin released membranes with very thick silicon supports, and the fluid

chamber. The DRIE process is also used to dice the wafer and provide fluid inlet and outlet ports. Finally, the thermal oxide is etched away using 1:1 HF and the dies are removed from the handle wafer using a positive resist stripper. A final clean is performed on the dies using Piranha (1:1 H_2SO_4:H_2O_2). At this stage, no thin gaps are present in the system, so when the device is dried there are no problems with stiction.

In parallel with the silicon processing, a 4 μm deep etch is performed on the Pyrex wafer using 3:1 HF with an evaporated Cr/Au etch mask. The height of these etched mesas determines the gap between the electrodes. The Cr/Au etch mask is removed using Au and Cr wet etchants, as shown in Figure 2 step 2b. The 20 nm Cr/ 100 nm Pt top electrode is then evaporated onto the Pyrex and patterned using liftoff. The 1.3 μm thick Sn solder is then evaporated onto the Pyrex, and also patterned using liftoff, resulting in the final structure shown in Figure 2 3b. The Sn provides the fluxless solder for the Sn-Au bond. The Pyrex wafer is then diced into individual dies, cleaned in acetone, isopropanol, and a DI water rinse, and dried in an oven. An unpatterned Pyrex wafer is also diced into 1.25 cm square dies for the chamber backsides.

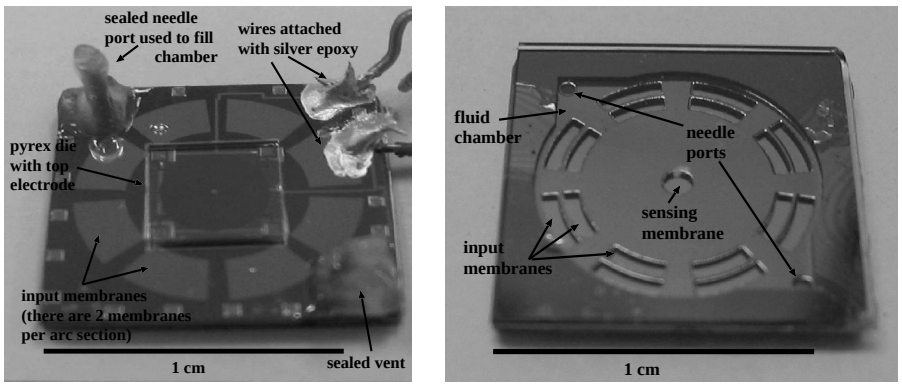

Figure 3. Photographs of the finished device. (a) Top view shows the outer ring of "input" membranes, the bonded Pyrex plate with top electrode, the fluid inlet and outlet, and the electrical connections made with silver epoxy. (b) Bottom view shows the fluid chamber, the "input" and "sensing" membranes, and the bottom side of the inlet and outlet ports.

Once all the dies are prepared, the unpatterned backside Pyrex dies are anodically bonded to the silicon dies at 350 C, 700 Volts for 30 mins. A custom bonding jig is used to make contact to the silicon die around the outsides, thereby avoiding damaging the fragile membranes, resulting in the structure shown in Figure 2 step 5. The topside, patterned Pyrex dies are then bonded to the silicon using Sn-Au solder bonding at 330 C for 30 mins in a N_2 ambient. A custom bonding jig is used to apply a light, uncalibrated clamping force during the bond. This results in the final structure shown in Figure 2 step 5.

In order to ensure electrical conductivity and mechanical strength of the Sn-Au bond, the temperature used during the bonding process is critical. If the temperature is too high, the Sn diffuses too rapidly into the Au on both sides of the bond, and the bond is weak. If the temperature is too low, the Sn-Au alloy will not form at all. A hotplate is used to perform the bond. The 330 C bonding temperature is measured by a thermocouple embedded in a 5 mm thick aluminum block between the hotplate surface and the die. It is expected that the actual temperature at the die surface will be somewhat (20-100 C) lower than the temperature measured by the thermocouple. For more details of Sn-Au bonding, see Goyal *et al.*[8] Measurements of the static capacitance after Sn-Au bonding (5.6 pF for a 2 mm diameter sense electrode) indicate a sensing gap of approximately 5 μm. This is approximately the total height of the spacers (Pyrex etch and thick Au) of 6 μm. In order to produce an open sensing gap (not shorted) it was critical to avoid any particles on either of the electrodes. Particles were generated mainly during the liftoff processing. The problem can be greatly mitigated by avoiding the use of ultrasonics. In addition, the use of Microposit 1112A, rather than acetone, as a liftoff solvent for both the Cr/Au and Cr/Pt reduced the particle count. Acetone was used for Sn liftoff due to chemical compatibility issues.

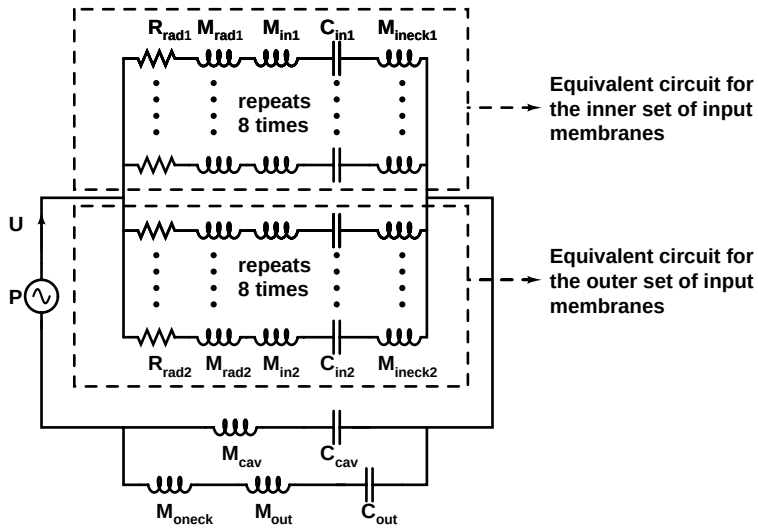

Figure 4. Equivalent acoustic circuit model for the system

In the final step, needles are epoxied into the needle fill ports which were etched during the DRIE steps. A micrometer injection jig is used to inject silicone oil into the fluid chamber. The needles are cut off and the inlet and outlet ports are sealed with epoxy. This step is not shown in Figure 2. The surfaces of the chamber are hydrophobic, so the silicone oil can be injected without the formation of many bubbles. The glass backside allows the chamber to be observed during filling, so any small bubbles that do form can be removed by continuing to flow silicone oil through the chamber until they are forced out. A photograph of the finished device is shown in Figure 3.

4. MODELING

Mathematical modeling of this system requires the solution of a coupled fluid structure problem. The fluid will be treated as a linear isotropic acoustic medium. The walls of the microchamber are modeled as rigid boundaries and only the membrane structures are taken to be flexible. The membrane is modeled as an isotropic tensioned membrane. Bending effects are neglected as tension dominates the structural elastic response. In the model, it is assumed that the structural response is linear. Time harmonic vibrations are considered. Two models are considered for the problem, an approximate low frequency model and a more detailed finite element model of the response.

4.1. LUMPED ELEMENT MODEL

At low frequencies where the hydrophone dimension is small compared to the wavelength of interest, a lumped parameter model is appropriate to approximate the sensitivity of the device.[1,2,9] An equivalent lumped acoustic element model for the hydrophone is shown in Figure 4. The input acoustic pressure of all 16 input membranes, P (assumed to be constant), and the total volume velocity of all 16 input membranes, U, are modeled as the potential (voltage) quantity and the flow(current) quantity, respectively.

In Figure 4, M_{rad1} and R_{rad1} are radiation mass and radiation resistance of one of 8 identical input membranes in the inner set, respectively. Similarly, M_{rad2} and R_{rad2} are those for the outer set. The radiation mass and resistance are determined by approximating the diaphragm as a plane piston mounted in an infinite baffle.[9] M_{ineck1} is the neck mass under one of inner membranes, and M_{ineck2} is the neck mass under one of outer membranes. M_{oneck} is the neck mass under the sensing membrane. For the neck, since one end of it is terminated in a large fluid cavity, the end correction is added to the neck mass.[9] The fluid cavity impedes the diaphragm movement by storing potential energy and has an equivalent compliance C_{cav}. The acoustic mass

M_{cav} for the cavity is also included in the circuit model. Expressions for all of these quantities can be found in a standard reference.[9]

C_{in1} and M_{in1} are acoustic compliance and mass for one of input membranes in the inner set. C_{in2} and M_{in2} are those for the outer set. The diaphragm compliance can be derived from the fundamental mode of the membrane vibration equation. For the input membrane, the fundamental mode and the first resonant frequency are obtained from a circular membrane equation,

$$T(\frac{\partial^2 \psi_{in1}}{\partial r^2} + \frac{1}{r}\frac{\partial \psi_{in1}}{\partial r} + \frac{1}{r^2}\frac{\partial^2 \psi_{in1}}{\partial \theta^2}) - \rho_m \frac{\partial^2 \psi_{in1}}{\partial t^2} = 0 \tag{1}$$

where T and ρ_m are the tension and the density of the membrane respectively. In order to satisfy the boundary conditions, the fundamental mode ψ_{in1} is,

$$\psi_{in1} = \sin \frac{\pi(\theta - \theta_1)}{\theta_2 - \theta_1}(c_1 J_n(k_{in1} r) + c_2 Y_n(k_{in1} r)) \tag{2}$$

where the ratio of c_1 to c_2 and the value of k_{in1} are determined by the boundary conditions $\psi_{in1}(r = r_1) = \psi_{in1}(r = r_2) = 0$. r_1 and r_2 are the inner and outer radii of the input membrane. θ_1 and θ_2 are the arc angles. J_n and Y_n are Bessel functions of the first and second kind of order $n = 6$. The first resonant frequency of the input membrane ω_{in1} is found from $\omega_{in1} = k_{in1}\sqrt{T/\rho_m}$.

Assuming the static deflection of the input membrane is $w_{in1} = A\psi_{in1}$, and substituting it into the static membrane equation,

$$T(\frac{\partial^2 w_{in1}}{\partial r^2} + \frac{1}{r}\frac{\partial w_{in1}}{\partial r} + \frac{1}{r^2}\frac{\partial^2 w_{in1}}{\partial \theta^2}) = P \tag{3}$$

we can solve for the modal coefficient A which depends linearly on the input pressure P,

$$A = -\frac{P\int_{r_1}^{r_2}\int_{\theta_1}^{\theta_2} \psi_{in1} r dr d\theta}{\rho_m \omega_{in1}^2 (\int_{r_1}^{r_2}\int_{\theta_1}^{\theta_2} \psi_{in1}^2 r dr d\theta)} \tag{4}$$

The input membrane compliance is then defined as the ratio of the volume displacement to the applied pressure,

$$C_{in1} = \frac{\int_{r_1}^{r_2}\int_{\theta_1}^{\theta_2} w_{in1} r dr d\theta}{P} = \frac{(\int_{r_1}^{r_2}\int_{\theta_1}^{\theta_2} \psi_{in1} r dr d\theta)^2}{\rho_m \omega_{in1}^2 (\int_{r_1}^{r_2}\int_{\theta_1}^{\theta_2} \psi_{in1}^2 r dr d\theta)} \tag{5}$$

The input membrane mass is computed from $M_{in1} = \frac{1}{C_{in1}\omega_{in1}^2}$. The value of C_{in2} and M_{in2} can be determined in similar fashion.

In Figure 4, M_{out} and C_{out} are acoustic mass and compliance of the sensing membrane. For the circular sensing membrane, the fundamental mode is $\psi_{out} = J_0(k_{out}r)$, where J_0 is the first kind Bessel function of order 0. k_{out} is determined from the boundary condition $\psi_{out}(r = r_{out}) = 0$, where r_{out} is the radius of the sensing membrane. The first resonant frequency ω_{out} is determined from $\omega_{out} = k_{out}\sqrt{T/\rho_m}$. Using the process described above, we can obtain the equivalent acoustic compliance and mass for the sensing membrane.

From the circuit, we can relate the volume velocity of the sensing membrane U_{out} to the total pressure input P,

$$\frac{U_{out}}{P} = \frac{Z_2}{Z_{out}(Z_2 + Z_{in1} + Z_{in2})} \tag{6}$$

where Z_{out} is the impedance of the sensing membrane and the neck under it. Z_{in1} is the impedance of the inner set of input membranes and the corresponding necks. Z_{in2} is the impedance of the outer set of input membranes and the corresponding necks. Z_2 is the equivalent impedance of the fluid cavity in parallel with Z_{out}. All the impedances are defined as,

$$\begin{aligned}
Z_{out} &= j\omega(M_{oneck} + M_{out}) + \frac{1}{j\omega C_{out}} \\
Z_2 &= \frac{Z_{out}}{1 + j\omega C_{cav} Z_{out}} \\
Z_{in1} &= \frac{1}{8}(j\omega(M_{rad1} + M_{ineck1} + M_{in1}) + \frac{1}{j\omega C_{in1}} + R_{rad1}) \\
Z_{in2} &= \frac{1}{8}(j\omega(M_{rad2} + M_{ineck2} + M_{in2}) + \frac{1}{j\omega C_{in2}} + R_{rad2})
\end{aligned}$$

By using the first kind Bessel function as the displacement distribution field in the sensing membrane, the center point displacement of w_{max} is related to the volume velocity U_{out} by $w_{max} = \frac{2.32}{j\omega A_{out}} U_{out}$, where A_{out} is the area of the sensing membrane. Figure 6 shows the predicted sensing membrane center point displacement sensitivity by the lumped model. It exhibits good agreement with the finite element model at low frequencies.

4.2. FINITE ELEMENT MODEL

A complete solution of the boundary value problem can be achieved numerically. This solution will be valid at higher frequencies than the lumped element model. With a numerical solution, it is also possible to explicitly include viscous fluid effects. As fluid viscosity is the dominant source of damping for the system, accurately modeling its effect is important, particularly near system resonances. A full three dimensional linearized Navier-Stokes fluid model produces a prohibitively large computational job. To avoid a three dimensional calculation, we take advantage of the size scales of the problem. In particular, the height of the fluid chamber is 20 times smaller than its diameter. Because of this, a two-dimensional thin film fluid model can be used. The derivation of the thin film fluid model is given by Beltman, *et al.*[10] The result is a modified Helmholtz equation,

$$\left[\frac{\partial^2 P}{\partial x_1^2} + \frac{\partial^2 P}{\partial x_2^2}\right] + \left(\frac{\omega}{c_{eff}}\right)^2 P = \frac{\rho_0 \omega^2}{h_0 B(\delta/h_0)} w_p \tag{7}$$

where $P = P(x_1, x_2)$ is the complex valued pressure field in the fluid chamber, $w_p = w_p(x_1, x_2)$ is the complex valued membrane displacement, and the remainder of the quantities are

$$
\begin{aligned}
B\Big(\frac{\delta}{h_0}\Big) &= 1 - \frac{\delta}{h_0}\frac{2(\cosh((j+1)h_0/\delta)-1)}{(j+1)\sinh((j+1)h_0/\delta)} \\
c_{eff} &= c_0\sqrt{B(\delta/h_0)} \\
\delta &= \sqrt{\frac{2\mu}{\rho_0\omega}}
\end{aligned}
$$

with viscous damping and structure coupling included. Viscosity enters by modifying the wave speed to a complex effective wavespeed, c_{eff}. The structural model is a tensioned membrane forced by the fluid pressure,

$$
T\frac{\partial^2 w_p}{\partial x_1^2} + T\frac{\partial^2 w_p}{\partial x_2^2} + m_a\omega^2 w_p = P \tag{8}
$$

In the equations, h_0 is the height of the fluid chamber. For regions underneath the membranes, h_0=500 μm. For regions underneath the silicon supports, h_0=300 μm. The density of silicone oil is taken to be ρ_0=950 kg/m^3, the free wave speed is c_0=1000 m/s, and the viscosity is μ=200 cSt. The membrane mass per unit area is computed from the bulk densities of the film materials and their thicknesses, resulting in m_a=5.4 g/m^2. The membrane tension is estimated from the stresses of the constituent films and their as-deposited thicknesses, giving T=70 N/m.

Equations 7 and 8 are the strong form of the boundary value problem and represent the fully coupled fluid-structure system. A standard Galerkin finite element procedure is used to solve the system. 4-noded isoparametric bilinear quadrilateral elements are used with a 2x2 Gaussian quadrature integration rule. Each node has two degrees of freedom: pressure and structure displacement. The system is complex, and all results are assumed to be time harmonic as $e^{j\omega t}$. The element stiffness matrix is symmetric.

A direct gauss elimination solver is used to invert the global stiffness matrix. Forcing to the system is provided by a vector of nodal forces acting on the structural degree of freedom. These forces can be conceptualized as a distributed pressure by integrating over the surface of application. A symmetry boundary condition is used along $x_1 = 0$ and $x_2 = 0$, as shown in Figure 5, producing a 1/4 size problem. Essential boundary conditions set the structural degree of freedom to zero over regions of the problem where the structure is very thick.

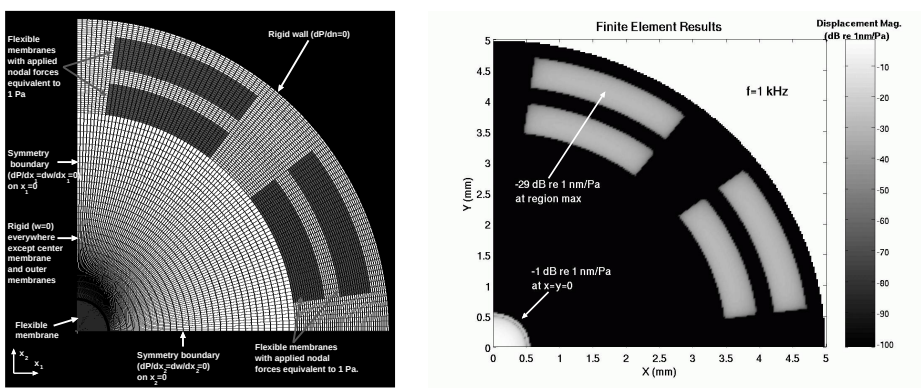

Figure 5. (a)Diagram showing the mesh and boundary conditions used for the finite element problem. (b) An example of the finite element result for structure displacement at 1 kHz. The geometry results in a 28 dB displacement gain between the outer membranes and the central membrane.

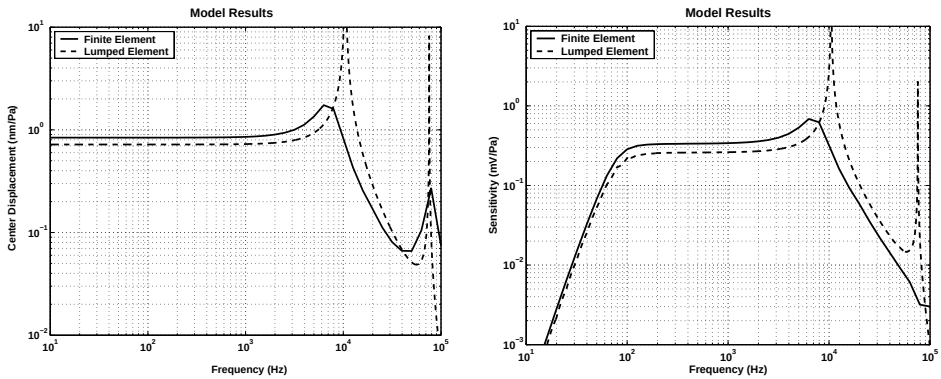

Figure 6. Model results showing good agreement for low frequency sensitivity and first resonant frequency between the finite element and lumped element models. (a) Predicted low frequency motion is approximately 1 nm/Pa, with the first resonance occurring at 7 kHz. (b) Based on the displacement results, the voltage sensitivity (including the model of the electronics) is expected to be 0.3 mV/Pa from 100 Hz-10 kHz.

4.3. ELECTRONICS

A simplified schematic of the system electronics is given in Figure 7. An AD795 low noise precision FET input operational amplifier is configured as a charge amplifier to integrate the charge generated by the MEMS sensor. A 10 pF silvered mica capacitor is used as the feedback capacitor and sets the charge gain of the system. A 200 MΩ feedback resistor is used to stabilize the system at DC. The RC cutoff frequency for this combination is 80 Hz. The 10 pF capacitor results in a 0.1 V/pC charge sensitivity. The output of the charge amplifier is passed through a 1 μF coupling capacitor into a bandpass filter circuit. The filter is constructed using a UAF42 universal active filter chip from Texas Instruments. The first stage is configured as a lowpass state-variable filter with a 2 pole cutoff at 70 kHz and a passband gain of 20 dB. The second stage is configured as a highpass voltage controlled voltage source with a 80 Hz cutoff frequency and 6 dB of passband gain. The net result of the entire system is a charge sensitivity of 2 V/pC in a 80 Hz - 70 kHz band[11] (b).

A DC bias, generated by an ADR01 bandgap reference IC, is applied across the plates of the MEMS sensor. A 10 kΩ potentiometer is used as a voltage divider to set the bias voltage anywhere from 0 to 10 V. For small deflections, the charge produced from the displacement of the sensor comes from the linearized change in capacitance multiplied by the applied DC bias voltage,

$$Q = V_{bias}\epsilon_0 \frac{1}{g_0^2} \int\int_A w_p(x,y)dxdy \tag{9}$$

where $g_0 = 5\mu m$ is the initial sense gap, $\epsilon_0 = 8.854 \cdot 10^{-12} F/m$ is the permittivity of free space, $w_p(x,y)$ is the displacement of the sense electrode, and the integral is over the area of the electrode. The resulting charge is then passed into the charge amp and through the filter transfer function to result in a final voltage output. Predicted sensitivity results are given in Figure 6.

5. EXPERIMENTAL RESULTS

A laser vibrometry system consisting of a Polytec OFV-303 sensor head, optics, and a 2D micropositioning stage is used to measure structural motion of the sensor. The device under test is mounted to the stage with wax. A speaker is attached to the stage (and is hence fixed relative to the device under test). A reference microphone is used to control the applied acoustic pressure to 100 dB re 20 μPa. A lockin amplifier measures the phase, relative to the microphone, and magnitude of the vibrometer velocity measurement at the driving frequency. A square region 2 mm on a side centered on the circular sensing membrane is measured in a 25 by 25 point grid.

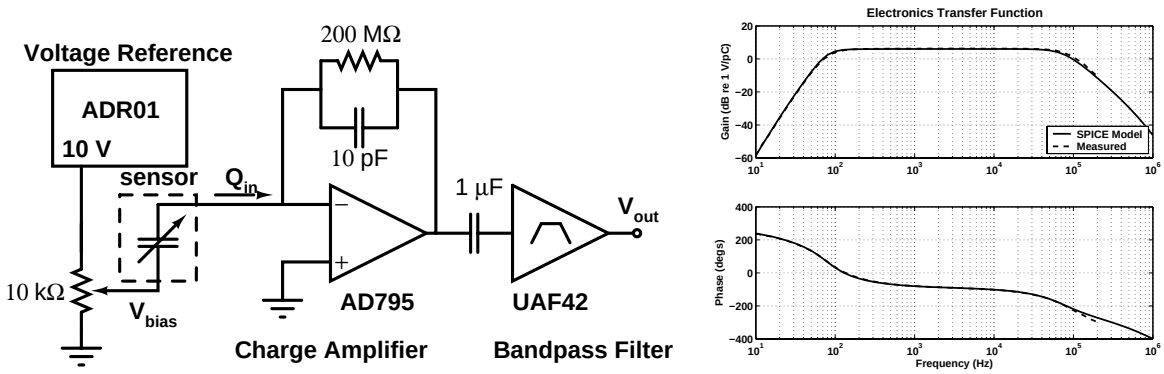

Figure 7. (a)Schematic of the system electronics, including DC voltage reference, charge amplifier, and bandpass filter. (b) Measured and modeled charge amp and bandpass filter characteristics (V_{out} vs Q_{in}.)

Figure 8 shows measurements of structural motion at two different frequencies. Below 5 kHz, the entire chip moves as a rigid body. The magnitude of motion at these frequencies is highly variable, with values from 0.1-4 nm/Pa. No relative motion is observed between the membrane and the edges of the chip. At frequencies between 5-20 kHz, the motion of the die edges reduces to approximately 0.1-0.3 nm/Pa, and the membrane responds in its first structural mode shape with amplitudes from 0.5-1 nm/Pa. At 22 kHz, the first antisymmetric mode is seen. The model predicts a modal frequency of 10-15 kHz for this mode, suggesting that the membrane tension is somewhat higher than anticipated. A higher tension would explain the extended bandwidth observed in the experimental results shown in Figure 9 (a).

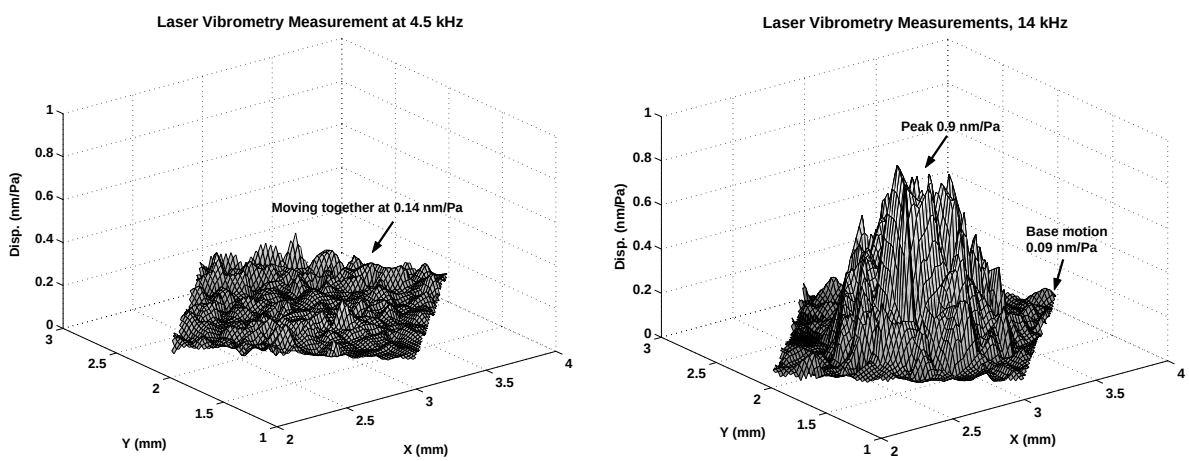

Figure 8. (a) Laser vibrometry measurements show little relative motion between the membrane and the body of the chip at frequencies below 5 kHz. At these frequencies, rigid body motion of the chip is highly variable, with magnitudes from 0.1-4 nm/Pa. (b) Above 5 kHz, the first structural mode shape is seen. The example presented is at 14 kHz, where membrane peak motion is 1 nm/Pa, with chip body motion of 0.1 nm/Pa. At these frequencies, membrane motion is always larger than chip body motion, and has magnitudes ranging from 0.5-1 nm/Pa.

Electrical sensitivity measurements are conducted with the MEMS chip mounted to the PC board electronics using wax. The board is mounted inside a grounded aluminum box. The box is partially lined with foam to damp acoustic resonances of the enclosure. A Larson-Davis 2520 0.25 inch diameter microphone with a 4 Hz to 60 kHz 3dB bandwidth is inserted into a cutaway hole through the back of the PC board to measure the delivered acoustic pressure. A speaker is driven closed loop by a computer to deliver 100 dB re 20 μPa across

a 300 Hz - 15 kHz band. The reference microphone is then replaced with the MEMS sensor, and an identical frequency sweep is conducted for a series of different bias voltages. At bias voltages above 2 V-2.5 V the sensor ceases to function. This is low for either to snapdown or to electrical breakdown of the air in the sense gap. The breakdown voltage for air is approximately $3{\cdot}10^6$ V/m, which would be 15 V with a 5 μm gap. For a 70 N/m tension in a 1 mm membrane with a 5 μm sense gap, the expected snapdown voltage is 75 V, based on an axisymmetric nonlinear finite difference solution to the governing equations.

Sensitivity measurements are given in Figure 9 (a). A 5 point moving average has been applied to smooth the results. At 1.5 V_{bias} the average sensitivity is 0.89 mV/Pa below 7 kHz, 0.32 mV/Pa above 7 kHz. With lower bias the sensitivity reduces proportional to the bias voltage as expected. With no bias a greatly reduced, but still measurable, signal is present, indicative of the level of "crosstalk" present in the data acquisition system. At frequencies below 7 kHz there is substantial fluctuation in sensitivity as a function of frequency. Above 7 kHz, the sensitivity curve has a reduced mean, and significantly reduced scatter, up to the maximum measured frequency of 15 kHz. Laser vibrometry measurements indicate that below 5 kHz there is considerable rigid body motion of the entire chip on the mounting wax. It seems likely that the fluctuations in sensitivity are due to these unmodeled and potentially complicated dynamics.

System noisefloor is given in Figure 9 (b). At frequencies below 10 kHz the noise exhibits a 1/f characteristic. Increasing DC bias increases the noise at low frequencies. The noise reaches a maximum at 100 Hz, below which it is attenuated due to the action of the bandpass filter.

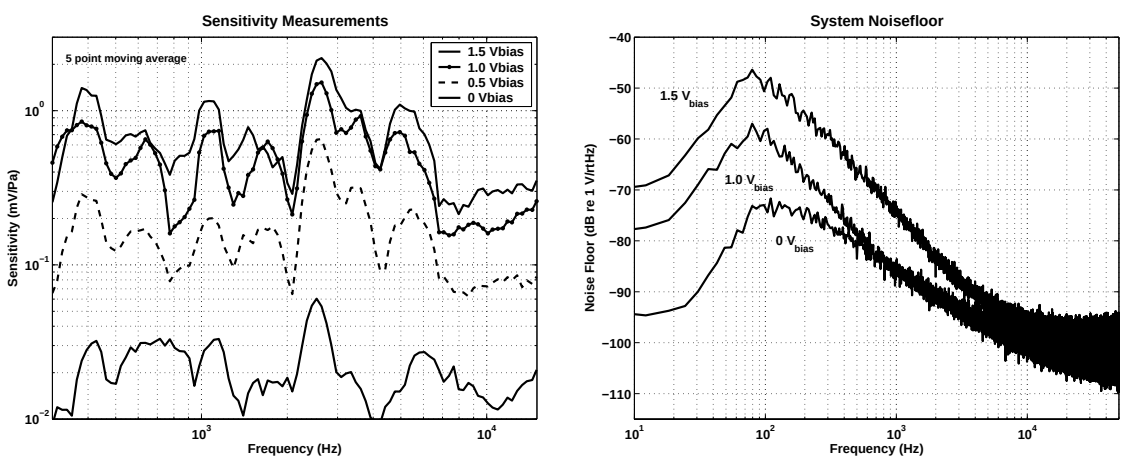

Figure 9. (a) Sensitivity measurements with different bias voltages. (b) Measurements of noise floor with different bias voltages.

6. SUMMARY

A unique geometry for a micromachined condenser hydrophone has been presented. A trapped fluid provides mass loading and damping. Models predict that this will allow the system to be submerged without affecting performance. The fluid chamber is also used to transmit pressure from a large "input" area to a smaller "sensing" area. Finite element results show a 28 dB displacement gain at low frequencies between the "input" and "sensing" membranes, which directly results in a 28 dB improvement in sensitivity. This ratio is the area ratio of the two sets of membranes. The displacement gain can be increased by continuing to increase the number of input membranes, as long as the total radial extent of the input membranes remains smaller than the free wavelength of sound in the environment.

Both lumped element and finite element model results predict approximately 1 nm/Pa deflection of the central membrane at low frequencies. This is the magnitude of membrane response observed with laser vibrometry between 5 kHz and 20 kHz. However, laser vibrometry measurements indicate that below 5 kHz the entire

chip oscillates, perhaps due to compliance of the supporting wax. Complexities in the dynamics of this unmodeled motion may be the cause of the variability in measured electrical sensitivity below 7 kHz. The predicted sensitivity with a 1.5 V applied bias and the described preamplifier circuitry is 0.3 mV/Pa in a 10 kHz band. Measurements show mean sensitivity of 0.9 mV/Pa from 300 Hz-7kHz, and 0.32 mV/Pa from 7 kHz-15kHz. No sensitivity measurements were made above 15 kHz.

Work is ongoing to improve packaging of the sensor. The mounting scheme for the sensor will be stiffened to remove low-frequency motion of the sensor on its supports, and thereby reduce the variability in low-frequency sensitivity. Secondly, the sensor will be packaged for submerged operation. This includes both sealing the electrical components away from the seawater and addressing issues of sensitivity to hydrostatic loading. Finally, electrical shielding will be incorporated to reduce crosstalk.

ACKNOWLEDGMENTS

Support for this work was provided by the Office of Naval Research, the National Science Foundation, and the University of Michigan.

REFERENCES

1. P. C. Hsu, C. Mastrangelo, and K. D. Wise, "A high sensitivity polysilicon diaphragm condenser microphone," *The Eleventh Annual International Workshop on MicroElectroMechanical Systems(MEMS '98)* , pp. 580–585, 1998.
2. W. Kuhnel and G. Hess, "A silicon condenser microphone with structured back plate and silicon nitride membrane," *Sensors and Actuators A* **30**, pp. 251–258, 1991.
3. P. R. Scheeper, B. Nordstrand, J. Gullov, B. Liu, T. Clausen, L. Midjord, and T. Storgaard-Larsen, "A new measurement microphone based on mems technology," *Journal of Microelectromechanical Systems* **12**, pp. 880–891, 2003.
4. P. R. Scheeper, A. G. H. vanderDonk, W. Olthius, and P. Bergveld, "Fabrication of silicon condenser microphones using single wafer technology," *Journal of Microelectromechanical Systems* **1**, pp. 147–154, 1992.
5. J. Bernstein, "A micromachined condenser hydrophone," *Solid-State Sensor and Actuator Workshop, 1992. 5th Technical Digest., IEEE* , pp. 161–165.
6. J. Zhang, A. Hladky-Hennion, W. Hughes, and R. Newnham, "Modeling and underwater characterization of cymbal transducers and arrays," *IEEE Transactions on Ultrasonics, Ferroelectrics, and Frequency Control* **48**, pp. 560–568, 2001.
7. S. Alkoy, J. Cochran, and R. Newnham, "Miniature hydrophones from hollow ceramic spheres," *Proceedings of the Eleventh IEEE International Symposium on Applications of Ferroelectrics* , pp. 345–348, 1998.
8. A. Goyal, J. Cheong, and S. Tadigadapa, "Tin-based solder bonding for mems fabrication and packaging applications," *Journal of Micromechanics and Microengineering* **14**, pp. 819–825, 2004.
9. L. L. Beranek, *Acoustics*, American Institute of Physics, Inc. New York, 1986.
10. W. M. Beltman, P. vanDerHoogt, R. Spiering, and H. Tijdeman, "Implementation and experimental validation of a new viscothermal acoustic finite element for acousto-elastic problems," *Journal of Sound and Vibration* **216**, pp. 159–185, 1998.
11. P. Horowitz and W. Hill, *The Art of Electronics*, Cambridge University Press, New York, 1980.